

Multigroup Thermal Radiation Transport with Tensor Trains

ADITYA S. DESHPANDE ^{1,2} PATRICK D. MULLEN ^{2,3} ALEX A. GORODETSKY ^{1,2} JOSHUA C. DOLENCE ^{2,3,1}
 CHAD D. MEYER ^{2,4} JONAH M. MILLER ^{2,3} AND LUKE F. ROBERTS ^{2,3}

¹*Department of Aerospace Engineering, University of Michigan, Ann Arbor, MI*

²*Michigan SPARC, Los Alamos National Laboratory, Ann Arbor, MI*

³*Computing and Artificial Intelligence, Los Alamos National Laboratory, Los Alamos, NM*

⁴*Continuum Models and Numerical Methods, Los Alamos National Laboratory, Los Alamos, NM*

Abstract

We investigate the application of tensor train (TT) algorithms to multigroup thermal radiation transport (i.e., photon radiation transport). The TT framework enables simulations at discretizations that might otherwise be computationally infeasible on conventional hardware. We show that solutions to certain multigroup problems possess an intrinsic low-rank structure, which the TT representation leverages effectively. This enables us to solve problems where the discretized solution size exceeds a trillion parameters on a single node. We consistently achieve compression factors $>100\times$ and speedups $>2\times$. The solver is evaluated across a range of test problems with varying levels of complexity. In addition, we further analyze the low-rank structure of the merged spatio-spectral core to evaluate the potential for additional compression via more advanced TT decompositions.

Keywords: Computational astronomy — Radiative transfer

1. INTRODUCTION

Frequency-dependent thermal radiation transport is central to a wide range of applications in astrophysics—including line-driven winds (e.g., I. Shlosman et al. 1985; D. Proga et al. 2000), black hole accretion (see, e.g., L. Zhang et al. 2025, and references therein), supernova explosions (e.g., R. A. Chevalier & C. Fransson 2008; R. T. Wollaeger et al. 2013; J. A. Goldberg et al. 2022), star formation (e.g., M. González et al. 2015; A. L. Rosen et al. 2016; A. L. Rosen & M. R. Krumholz 2020; S. H. Menon et al. 2023), gamma-ray bursts (e.g., C. Thompson 1994; J. Zrake et al. 2019; V. Nedora et al. 2025), tidal disruption events (e.g., X. Huang et al. 2025; I. Giron et al. 2026), and X-ray pulsars (see, I. Caballero & J. Wilms 2012, and references therein)—as well as in nuclear science and engineering, particularly inertial confinement fusion (ICF; B. M. Haines et al. 2022; Y. Kim et al. 2023).

The radiation transport equation for photons governs the specific intensity I_ν , a quantity defined over space, propagation direction, and frequency. This intrinsic high dimensionality renders first-principles numerical solutions extremely expensive, motivating a hierarchy of approximations that reduce angular and/or spectral resolution. One common simplification is the gray approximation, in which frequency dependence is removed by integrating the intensity over the entire spectrum. While this eliminates one dimension of the problem, it implicitly assumes that frequency-dependent opacity effects can be well represented by suitable averages. Multigroup radiation transport (MRT) relaxes this assumption by discretizing the frequency domain into a finite set of groups, retaining limited spectral resolution while remaining computationally tractable. However, even within the multigroup framework, solving the transport equation directly remains a challenge. Discrete ordinates S_N methods require resolving the angular domain with many directions (to eliminate so-called “ray effects”; see, e.g., A. A. Gorodetsky et al. 2025) and the spectral domain with multiple frequency groups, leading to a rapid growth in the total number of required parameters to store the solution. This burden is further amplified by the need for fine spatial discretizations in many applications—for example, to accurately resolve material interfaces, shocks, or fluid instabilities—thereby exacerbating the curse of dimensionality.

This curse of dimensionality is particularly severe in applications such as line-driven transport and indirect-drive inertial confinement fusion (ICF). In stellar and active galactic nuclei (AGN) winds, the line-driving force arises from interactions with many ultraviolet resonance lines (D. Proga 2007). The cumulative radiative force depends sensitively on how the radiation field samples a dense forest of line opacities as a function of frequency. Accurately representing

this physics directly in the transport equation requires a finely resolved frequency grid to capture overlapping lines and ionization-dependent features, often necessitating hundreds to thousands of frequency groups in the UV alone. In ICF hohlraums, X-ray drive and wall re-emission involve complex, strongly frequency-dependent opacities with sharp edges and line features associated with high-Z materials (V. Tolkach et al. 2003). Capturing non-gray effects in absorption, re-emission, spectral shaping, drive symmetry, and capsule preheat requires MRT with tens to hundreds of energy groups.

To make MRT problems computationally tractable, existing S_N calculations typically have been limited to relatively few groups, few angles, short runtimes, and/or limited spatial resolutions (e.g., A. Secunda et al. 2024; B. S. Mills et al. 2024; A. Secunda et al. 2025; Y.-F. Jiang et al. 2025; H. Liu et al. 2025; X. Huang et al. 2025). More commonplace, an alternative approach to mitigating the inherent dimensionality of the transport equation is to evolve angle-integrated quantities using moment-based methods. Such approaches have been extended to the multigroup setting, including flux-limited diffusion FLD and M1 models (see, e.g., R. Wünsch 2024, for a nice review). However, like their gray counterparts, these methods suffer from limitations associated with angular averaging. In addition to invoking moment-based methods, contemporary ICF simulations also frequently reduce dimensionality by restricting the spatial geometry to one- or two-dimensional settings. In the context of line-driven winds, D. Proga et al. (1999) replaces full transport with so-called “force multiplier” models.

In this work, we propose to address the curse of dimensionality by incorporating tensor-trains (TT, I. V. Oseledets 2011) into a multigroup transport solver. Tensor-train representations have been successfully applied to gray thermal transport (A. A. Gorodetsky et al. 2025), and were able to reproduce analytical solutions across numerous test cases while achieving speedups and compression factors of $\sim 60\times$ and $\sim 1000\times$, respectively. This naturally raises the question of whether solutions to the MRT equations also exhibit low-rank structure and can similarly be represented efficiently using TTs. We explore this question by developing a multigroup TT solver. Additionally, given the many possible tensor-network representations of the solution, we also investigate alternative TT topologies and compare their performance. The remainder of the paper is structured as follows. §2 presents the MRT equations and outlines the numerical algorithm, while §3 details the tensorization of the solver. We conduct a series of multigroup test problems to assess the solver in §4 followed by an extensive discussion in §5. §6 concludes the work with a summary of our findings.

2. GOVERNING EQUATIONS

The time evolution of the frequency-dependent specific intensity I_ν is governed by the transport equation

$$\partial_t I_\nu + c\mathbf{n} \cdot \nabla I_\nu = c(j_\nu - \alpha_\nu I_\nu), \quad (1)$$

where c is the speed of light, \mathbf{n} is a unit normal defining photon propagation direction, and j_ν and α_ν denote the frequency-dependent emissivity and absorptivity, respectively.

In the multigroup formalism, the frequency domain is divided into N_ν bins. End points $\nu_0, \nu_1, \dots, \nu_{N_\nu}$ with $\nu_0 = 0$ and $\nu_{N_\nu} = \infty$ cover the entirety of frequency space. Integrating the transport equation over a frequency bin f with frequency bounds $[\nu_{f-1}, \nu_f]$ results in

$$\partial_t I_f + c\mathbf{n} \cdot \nabla I_f = c(j_f - \alpha_f I_f), \quad (2)$$

where the f subscript denotes a group integrated quantity (e.g., $I_f = \int_{\nu_{f-1}}^{\nu_f} I_\nu d\nu$ is the frequency-integrated specific intensity in bin f) and α_f is assumed to be an average over the group.⁵

Assuming a static background medium (with material mass density ρ and temperature T), local thermodynamic equilibrium (LTE), and isotropic, elastic scattering, we can expand the multigroup transport equation as

$$\partial_t I_f + c\mathbf{n} \cdot \nabla I_f = c[\rho\kappa_{s,f}(J_f - I_f) + \rho\kappa_{a,f}(\varepsilon_f - I_f)], \quad (3)$$

where $\kappa_{a,f}$ and $\kappa_{s,f}$ are the specific group mean absorption and scattering opacities, respectively, J_f is the group mean intensity over solid angle Ω (related to the group radiation energy density via $E_f = \frac{4\pi}{c} J_f = \frac{1}{c} \int I_f d\Omega$), and ε_f is an

⁵ Planck or Rosseland averaging could be employed in constructing group mean opacities. For simplicity, we do not augment the transport equation to include *both* Planck and Rosseland opacities as done in Y.-F. Jiang (2022), which would otherwise amount to an additional contribution to the coupling source term.

emission coefficient proportional to the integral of the Planck function $B(\nu, T)$ over $[\nu_{f-1}, \nu_f]$

$$\varepsilon_f = \frac{c}{4\pi} \int_{\nu_{f-1}}^{\nu_f} B(\nu, T) d\nu, \quad \text{where} \quad (4)$$

$$B(\nu, T) = \frac{8\pi h\nu^3}{c^3} \frac{1}{\exp(h\nu/[kT]) - 1}. \quad (5)$$

For a single group with $[\nu_0, \nu_{N_\nu}] \rightarrow [0, \infty)$ (i.e., “gray”), ε_f reduces to $\varepsilon_{\text{gray}} = caT^4/[4\pi]$, where a is the radiation constant.

Radiation feedback on a fluid is determined via conservation of total energy hence giving rise to a material temperature equation

$$\partial_t T = - \sum_f \left[\frac{c\kappa_{a,f}}{c_v} \left(\frac{4\pi}{c} \varepsilon_f - E_f \right) \right]. \quad (6)$$

2.1. Numerics

In this work, the [A. A. Gorodetsky et al. \(2025\)](#) thermal radiation transport with tensor trains (TTTT) solver is extended to multigroup. We highlight here only the modifications to the numerical algorithm that pertain specifically to transitions between the gray and multigroup formalisms.

The transport operator is evolved explicitly using the same three flux stencils from [A. A. Gorodetsky et al. \(2025\)](#): upwinding, Rusanov ([E. F. Toro 2009](#)), and the asymptotic-preserving, HLL flux of [Y.-F. Jiang \(2021\)](#). The introduction of multigroup changes only the HLL stencil, which now invokes an optical depth per frequency bin $\tau_{c,f}$ (see later, §3)—wavespeeds are otherwise computed identically. We advance the right hand side of Equation (3) from time index m to $m + 1$ via a backward Euler, operator split update,

$$\frac{I_f^{m+1} - I_f^m}{c\Delta t} = \rho^m \kappa_{s,f}^m (J_f^{m+1} - I_f^{m+1}) + \rho^m \kappa_{a,f}^m (\varepsilon_f^{m+1} - I_f^{m+1}), \quad (7)$$

$$\frac{T^{m+1} - T^m}{c\Delta t} = - \sum_f \left[\frac{\kappa_{a,f}^m}{c_v^m} \frac{4\pi}{c} (\varepsilon_f^{m+1} - J_f^{m+1}) \right], \quad (8)$$

where $\kappa_{a,f}$ and $\kappa_{s,f}$ are assumed to be constant over the coupling stage. Integrating Equation (7) over solid angle gives an advanced mean intensity that can be substituted into Equation (8) to arrive at a polynomial

$$f(T^\dagger) \equiv T^m - T^\dagger - \sum_f \left[\frac{4\pi\Delta t \kappa_{a,f}^m}{c_v^m} \left(\varepsilon_f(T^\dagger) - \left(\frac{1}{[c\Delta t]^{-1} + \rho^m \kappa_{a,f}^m} \right) \left(\frac{J_f^m}{c\Delta t} + \rho^m \kappa_{a,f}^m \varepsilon_f^\dagger(T^\dagger) \right) \right) \right] \quad (9)$$

where the physical root gives an advanced stage temperature T^\dagger (and hence emission coefficient $\varepsilon_f[T^\dagger]$) to implicitly advance the specific intensity I_f . Rather than advancing the temperature via $T^{m+1} = T^\dagger$, we invoke total energy conservation

$$\rho^m c_v^m (T^{m+1} - T^m) = \frac{4\pi}{c} \sum_f \left[J_f^m - \frac{1}{4\pi} \sum_{\ell,p} I_{f\ell p}^{m+1} \Delta\Omega_{\ell p} \right]. \quad (10)$$

to govern the feedback of the radiation field on the fluid.

The integrals of the Planckian used in constructing $\varepsilon_f[T]$ have analytic solutions that are complicated functions of polylogarithms. We adopt the efficient polylogarithm evaluation strategy following [A. Voigt \(2022, 2023\)](#) and [M. Roughan \(2020\)](#), which enables rapid computation of polylogs of orders 2, 3, and 4 with accuracies approaching machine precision.

3. TENSORS

A key contribution of this paper is the development of a tensorized version of a “traditional” MRT solver, which enables the solution of multigroup problems at discretizations that would be challenging (if not impossible) for conventional methods. The multigroup specific intensity solution has $N_X N_\nu N_\theta N_\phi$ unknowns, where N_X is chosen represent the *total* number of spatial coordinates (= N_x , $N_x N_y$, and $N_x N_y N_z$ for 1D, 2D, and 3D, respectively). N_ν represent

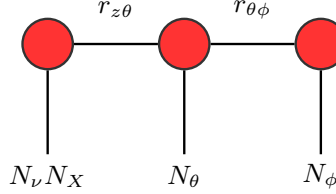


Figure 1. Graphical representation of the TT solution.

the number of groups (i.e., frequency “bins”) and $N_\theta N_\phi$ is the total number of angles in a latitude/longitude (θ, ϕ) discretization, forming a 2D tensor product angular space. We represent the specific intensity solution in a TT format as

$$\hat{I}_{k\ell p} = Z_k \Theta_\ell \Phi_p. \quad (11)$$

Here, $Z \in \mathbb{R}^{N_X N_\nu \times r_{z\theta}}$ represents a core that combines the spatial and frequency dimensions (i.e., a “spatio-spectral” core), while $\Theta \in \mathbb{R}^{r_{z\theta} \times N_\theta \times r_{\theta\phi}}$ and $\Phi \in \mathbb{R}^{r_{\theta\phi} N_\phi}$ represent the angular cores. $r_{z\theta}$, $r_{\theta\phi}$ are the TT ranks. Figure 1 illustrates a graphical visualization (J. Biamonte & V. Bergholm 2017) of the TT solution.

We refer the reader to A. A. Gorodetsky et al. (2025) for a review of the basic TT operations such as addition, integration, multiplication, and rounding. We re-emphasize that TT-operations assume compatibility between operands. For example, if wanting to add/multiply the solution \hat{I} with a spatio-spectral quantity like the opacity κ , the operation requires both \hat{I} and κ to have the same format. Specifically, if \hat{I} is represented as in Equation (11), then the TT form of the opacity $\hat{\kappa}$ should be represented as $\hat{Z}_k \hat{\Theta}_l \hat{\Phi}_p$ where $\hat{Z} = \kappa$ and $\hat{\Theta}, \hat{\Phi}$ are rank-1 cores filled with 1 in order to artificially increase the dimensionality of the opacity. Any discrepancy in the formats of operands needs to be resolved via preprocessing before carrying out the operation.

All flux stencils studied in A. A. Gorodetsky et al. (2025) can be straightforwardly extended to the multigroup setting. The upwind flux and Rusanov fluxes (as presented in A. A. Gorodetsky et al. 2025) are independent of the local group opacity and therefore follow the same implementation as their gray counterpart. The HLL interface flux is a function of the local optical depth $\tau_{c,f}$ that is a function of *both* space and frequency, however, because we have opted for a *merged* spatio-spectral core, tensor arithmetic in constructing the HLL flux is immediately straightforward (i.e., the tensor formats are compatible). Alternative, more advanced tensor decompositions may not benefit from such simplicity (see §4). The source solver presents similar considerations as HLL flux operator. In evaluating the advanced specific intensity I^{m+1} , $\kappa_{a,f}$, $\kappa_{s,f}$, and ε_f^\dagger equally vary with space and frequency. Consequently, addition and multiplication in the implicit update benefit from the unified spatio-spectral core employed in this work.

Nonetheless, we concede that our representation does not fully leverage separability between the spatial and spectral dimensions, which may manifest as additional low-rank structure within the core Z . This internal structure could be leveraged for greater compression for certain multigroup problems. We quantify the internal structure with the help of internal ranks and study their behavior in §5. To summarize, the multigroup TTTT solver advances the TT solution via a step-then-truncate algorithm, in which the transport operator is advanced, followed by the source-term step, and finalizing with a rounding operation after each solve to control rank growth.

4. TEST PROBLEMS

Building on the results of A. A. Gorodetsky et al. (2025), we anticipate that the TTTT solver will achieve substantial compressions and speedups relative to “traditional” multigroup S_N implementations. Herein, for representative multigroup test problems, we assess the rank structure of the tensor decomposition employed in this work. We define the compression ratio

$$\mathcal{C} := \frac{N_{\text{trad}}}{N_{\text{TT}}} = \frac{N_X N_\nu N_\theta N_\phi}{N_X N_\nu r_{z\theta} + N_\theta r_{z\theta} r_{\theta\phi} + N_\phi r_{\theta\phi}} \quad (12)$$

which compares the traditional multigroup storage requirement to the TTTT one. We also define the speedup \mathcal{S} as the ratio of the time taken by a traditional solver to the time taken by the TT-solver.⁶ We also introduce some metrics associated with the internal structure of Z in §5. These along with \mathcal{C} and \mathcal{S} dictate the performance of our solver and are reported for all test problems alongside the rounding tolerances inside Table 2.

We adopt custom unit systems for all tests except Graziani's test (which enrolls cgs units). In the multigroup tests, these modified units are taken from the corresponding gray versions described in [A. A. Gorodetsky et al. \(2025\)](#). We note that the choice of unit system can affect solution accuracy, potentially due to floating-point effects, and as with all numerical methods, a unit system where the magnitude of the solution is of order unity is ideal. Lastly, following [C. J. White et al. \(2023\)](#) and [A. A. Gorodetsky et al. \(2025\)](#), we select $N_\phi = 2N_\theta$ for our latitude/longitude angular discretization and unless otherwise specified, we consider $\nu_1, \nu_2, \dots, \nu_{N_\nu-1}$ to be logarithmically spaced, with $\nu_0 = 0$ and $\nu_{N_\nu} = \infty$.

4.1. Multigroup Hohlraum

We begin by assessing the multigroup TTTT solver's performance in the free streaming limit via the 2D hohlraum vacuum transport problem ([B. R. Ryan & J. C. Dolence 2020](#); [C. J. White et al. 2023](#); [A. A. Gorodetsky et al. 2025](#)). A square spatial domain is discretized into $N_X = 128^2$ cells. We choose $N_\theta \times N_\phi = 512 \times 1024$ angles to reduce errors from ray effects and invoke an upwinded flux. Fixed left and bottom isotropic boundary sources with frequency integrated specific intensity $I = J = 1$ send radiation propagating throughout the domain.

We adapt the problem to multigroup as follows. The frequency domain is discretized into $N_\nu = 10$ bins. The isotropic boundaries at the left and bottom are initialized in two ways (1) $I_f = J_f = 1/N_\nu$ and (2) $I_f = J_f = \varepsilon_f(T_{\text{init}})$ such that $a_r T_{\text{init}}^4 = 4\pi/c$. The former setup sets each group identically, and each group should evolve identically; the second setup will have each group propagate identically, but with a magnitude set by the initial thermal spectrum at the active boundaries. Both setups have an analytic result derived from the gray solutions in [C. J. White et al. \(2023\)](#) and [A. A. Gorodetsky et al. \(2025\)](#), which we do not repeat here.

We explore both configurations to demonstrate interesting properties of our solver. We plot the TT-rank evolution in Figure 2 and observe that both initializations present identical rank evolution even though the distributions of specific intensity across the frequency domain are different. This stems from the fact that frequency only influences the solution through a group-dependent constant that scales the gray solution. Consequently, the rank evolution for the chosen discretization should remain unchanged even if the intensities in different groups are initialized randomly.⁷

Figure 3 compares the analytical and numerical solutions for $\sum_f J_f$ for both cases at $t = 0.75$. For both cases, the TTTT solver recovers the gray analytics (albeit exhibiting large 1st order spatial truncation errors) and presents a total compression ratio of $\mathcal{C} \approx 5150$ and a speedup of $\mathcal{S} \approx 60$.

Finally, we remark that the decoupling of frequency dimension in the solution hints at rank-1 structure inside Z and suggests potential for additional compression gains by separating the frequency core (see later discussion in §5.2).

4.2. Thermal Relaxation

Moving beyond vacuum transport, the multigroup thermal relaxation test problem investigates a frequency-dependent problem invoking the absorption and emission source terms and radiation feedback ([Y.-F. Jiang 2022](#)). In this test, a material and radiation are initialized to different temperatures (T and T_r) inducing energy exchange among them until thermal equilibrium is reached. Each group evolves on a timescale determined by its group opacity $\kappa_{a,f}$. The final equilibrium temperature T_{eq} is independent of group structure ν_f and opacity structure $\kappa_{a,f}$, and is derived from total energy conservation (see, e.g., [A. A. Gorodetsky et al. 2025](#)).

We consider $\rho = 1$, $c_v = 8$, $T_{\text{initial}} = 10$, $T_{r,\text{initial}} = 1$ and adopt a unit system wherein $a = c = 1$. Note that the resulting equilibrium temperature for these settings is $T_{\text{eq}} \simeq 2.77$. We choose $N_X = 4$ cells to span the spatial domain of extent $[0, 4]$. We use $N_\theta \times N_\phi = 512 \times 1024$ angles and initialize the mean intensity for each group as $J_f = \varepsilon_f(T_{r,\text{initial}})$. We highlight that the choice of spatial and angular discretization is immaterial, since the solution in each group remains isotropic and spatially uniform, reducing the problem to one that depends solely on frequency. Although the numerical flux choice is inconsequential, we invoke the Rusanov flux with $S^+ = c$ for this test.

⁶ For the traditional solver baseline, we adopt the same performance metric from [A. A. Gorodetsky et al. \(2025\)](#), but now run on a Mac Mini — vacuum transport: 5.0×10^8 , scattering: 3.7×10^8 , absorption/emission: 3.6×10^8 degrees of freedom updates per second. We assume perfect scaling of the gray solver with number of groups—an aggressive upper limit given multigroup introduces nontrivial Planckian integral evaluations.

⁷ This assumes spatially uniform and groupwise-identical left and bottom boundary conditions. For instance, initializing the left and bottom boundaries with distinct values of T_{init} would lead to a different TT-rank behavior compared to our two included cases.

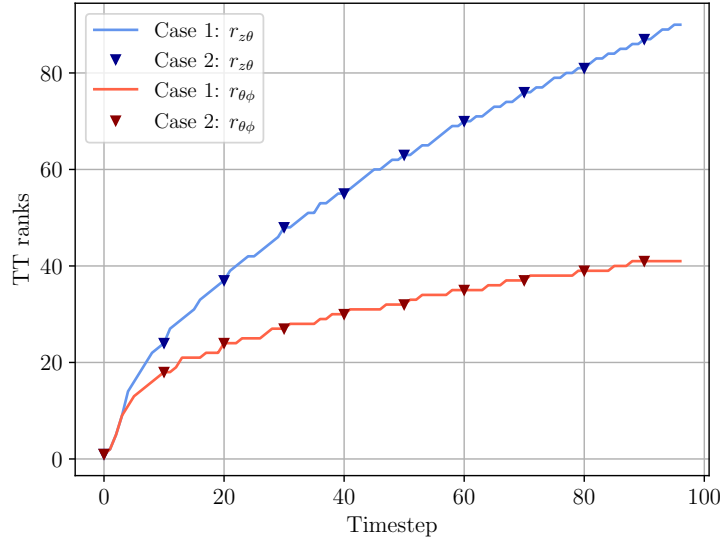


Figure 2. Rank evolution of the multigroup hohlraum problem for both cases. The plot reveals that the rank evolution stays the same for both cases despite the discrepancy in initialization. We attribute this to the fact that the solution in every bin evolves exactly according to the gray solution scaled by the initial intensity in that bin. This leaves the TT-ranks unchanged for arbitrary intensity initializations across the frequency domain.

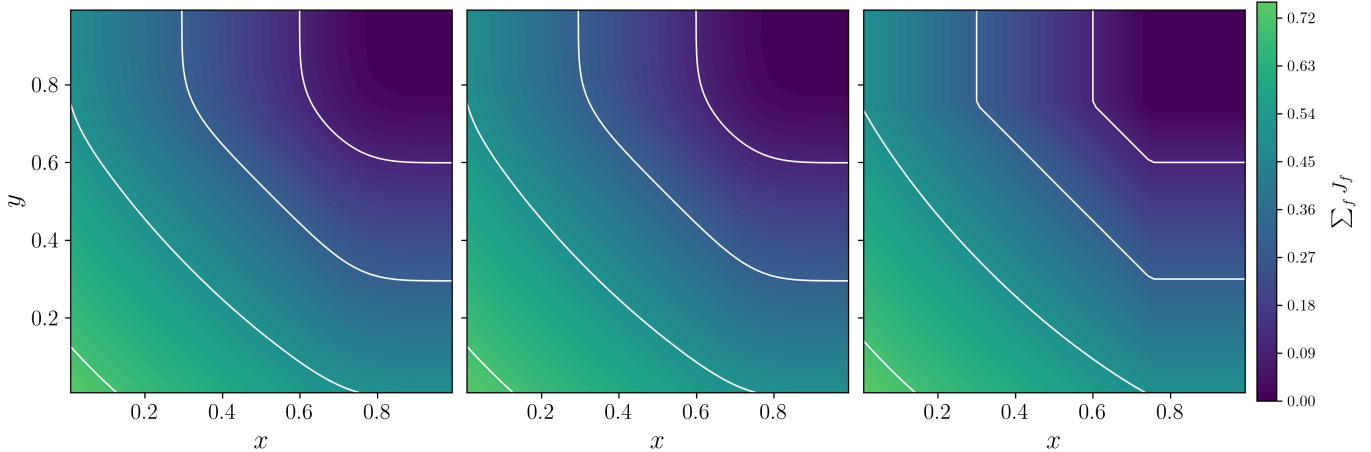


Figure 3. Reduction of multigroup mean intensities to the gray case for case 1 (left) and 2 (center) plotted alongside the corresponding analytics (right) at $t = 0.75$. Plots are overlayed with white contour lines at $\sum_f J_f = [0.1, 0.3, 0.5, 0.7]$. The numerical solution follows the analytical solution closely with compression and speedup amounting to ~ 5150 and ~ 73 respectively.

4.2.1. $N_\nu = 3$

We test the solver for $N_\nu = 3$ with $\nu_1 = k$ and $\nu_2 = 2k$ where $k = 1.5 \times 10^{11}$. We set $\kappa_{a,1} = 10$, $\kappa_{a,2} = 1$, $\kappa_{a,3} = 0.1$ and run the solver to $t_{\text{final}} = 40$. We normalize the radiation energy density by aT_{eq}^4 and denote it by \bar{E}_f .

The analytic equilibrium states for this problem are $\bar{E}_1 = 0.3$, $\bar{E}_2 = 0.35$, and $\bar{E}_3 = 0.34$. The numerical solution is presented in Figure 4 where we plot the time evolution of \bar{E}_f for $f = 1, 2, 3$ along with $\sum_f \bar{E}_f$. The solutions converge to and match the analytics in every group signifying that the solver works as expected. We observe that the path to equilibrium varies across groups. Groups with higher opacities exhibit rapid changes in \bar{E}_f during the early stages and dominate the temperature evolution of the medium at these times. As the temperature evolves, additional groups become active.

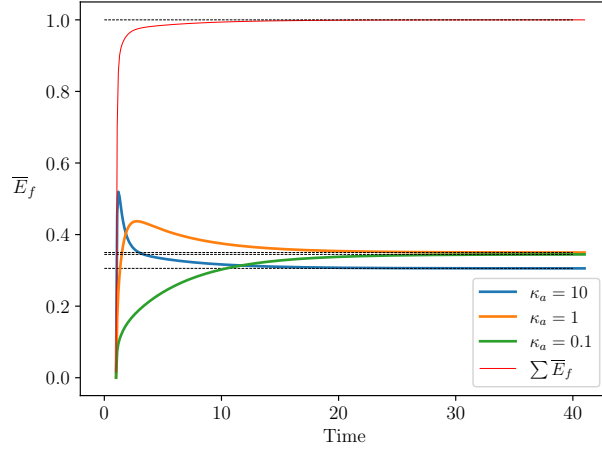


Figure 4. Plot of the normalized radiation energy \bar{E}_f v/s time. Different colored lines represent the solution evolution in different frequency groups and each plot converges to analytics as thermal equilibrium (at $T = T_{eq}$) is achieved.

4.2.2. $N_\nu = 100$

To test the robustness of the implementation, we consider a case with $N_\nu = 100$. The group opacities are assigned using a random number generator such that $\kappa_{a,f} = 10^x$, where x is uniformly sampled from the interval $[-2, 2]$ (see Figure 5a). The system is evolved up to time $t_{final} = 10$.

We visualize the solution in the included movie as a time-dependent spectrum, plotting J_f versus frequency ν . Initially, the material and radiation spectra are given by $\varepsilon_f(T_{initial})$ and $\varepsilon_f(T_{r,initial})$, respectively. As the system evolves, both spectra relax toward a Planck distribution corresponding to the equilibrium temperature T_{eq} , i.e., $\varepsilon_f(T_{eq})$. We observe each group evolving at a rate proportional to its respective opacity $\kappa_{a,f}$ (albeit each group must settle before T_{eq} is achieved).

Alternatively, the solution can also be visualized as an energy versus time plot as shown in Figure 5b. We plot the evolution of gas energy (blue) and total radiation energy (green). The radiation energy in various bins is plotted and colored according to the value of opacity in the bin. The dynamics here are fundamentally the same as in the previous test, though they now appear far more complex. Even still, the solver captures the temperature variation for each group and demonstrates perfect compression. At all times, the thermal relaxation solution admits a rank-1 TT representation, yielding compressions of $\mathcal{C} = 4000$ when $N_\nu = 3$ and $\mathcal{C} = 1.2 \times 10^5$ when $N_\nu = 100$.

The extent to which compression improves with increased spectral resolution depends on both the TT ranks and the sizes of the TT cores. The thermal relaxation problem represents a best-case scenario with respect to the former, as it yields a rank-1 solution. Consequently, the substantial increase in compression observed when increasing from $N_\nu = 3$ to $N_\nu = 100$ is not generally applicable to other problems or even to different resolutions of the same problem. In cases that produce higher-rank solutions, the gain in \mathcal{C} with increasing N_ν is more modest. Moreover, for the present problem, this increase would be significantly smaller if $N_X N_\nu \gg N_\theta, N_\phi$.

4.3. Gaussian diffusion

In this problem, an initial 1D Gaussian pulse is diffused at a rate inversely proportional to the scattering opacity of the medium. To extend this to multigroup, we simply assign different scattering opacities to different groups and probe the TT-ranks of the solution over time. The analytics for the radiation energy density are given by

$$E_f(t, x; t_0) = \frac{A}{\sqrt{4\pi D_f(t_{0,f} + t)}} \exp \left[-\frac{x^2}{4D_f(t_{0,f} + t)} \right], \quad (13)$$

where A denotes the initial Gaussian amplitude, and both the initial time $t_{0,f}$ and the scattering diffusion coefficient $D_f := c/(3\rho\kappa_{s,f})$ can be group dependent (M. D. Sekora & J. M. Stone 2010; Y.-F. Jiang et al. 2014; Y.-F. Jiang 2021).

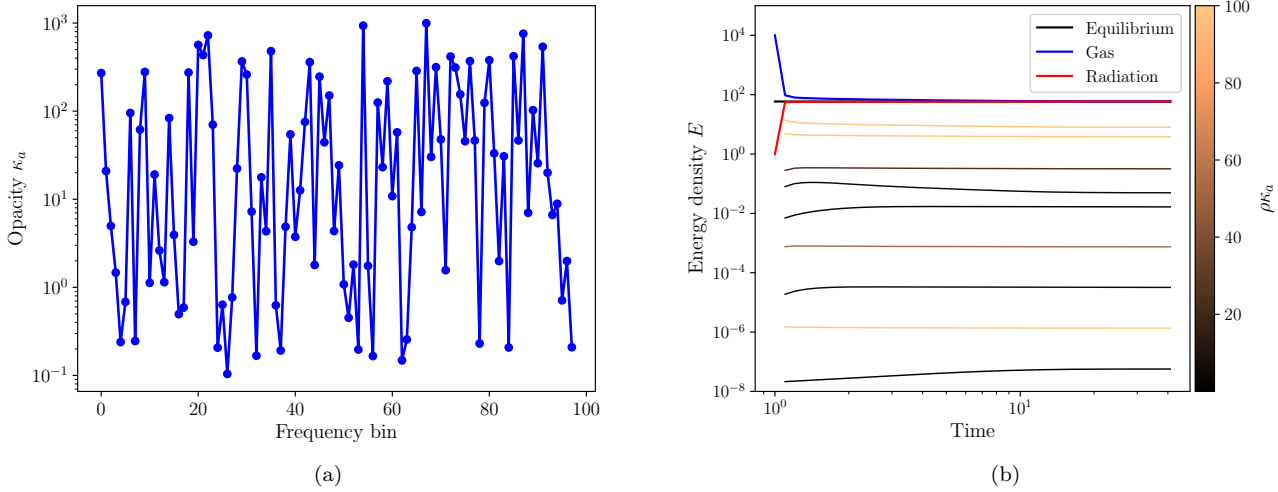


Figure 5. (a) Opacities $\kappa_{a,f}$ for the $N_f = 100$ relaxation test. (b) The variation of thermal energy density of the material ($\rho c_v T$) (blue), radiation energy density for some of the groups (colorbar), and the total radiation energy density (red) with time. The numerical solutions converge to the predicted analytic equilibrium. Notice that the radiation energy density generally reaches a steady value slower for groups with lower opacities (the darker lines flatten later compared to the orange ones).

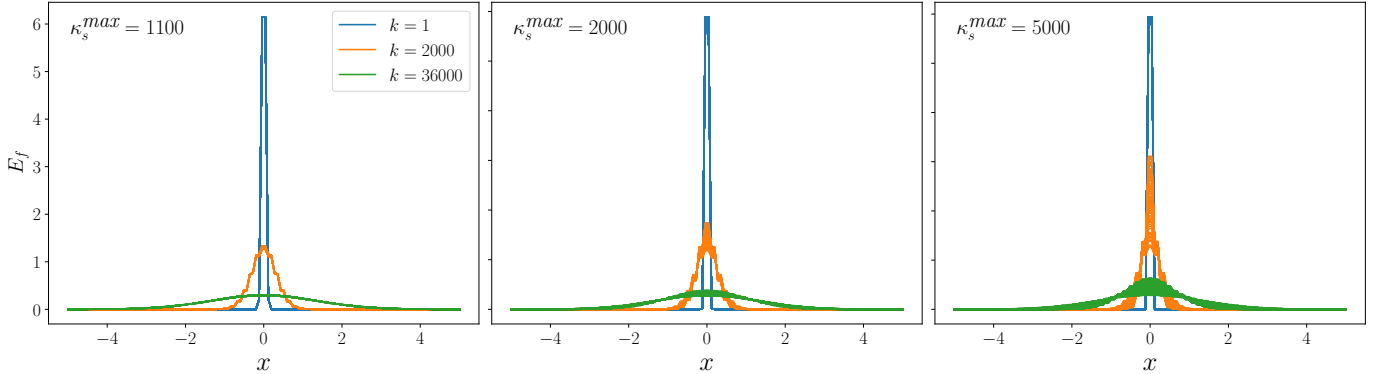


Figure 6. Radiation energy density snapshots for *all* frequency groups at timesteps $k = 1, 2000$, and 36000 (blue, orange, and green, respectively), shown for increasing values of κ_s^{\max} from left to right. Initially, the solution is identical across groups, producing an overlapping set of Gaussian profiles. As time evolves, the groupwise solutions diverge due to differences in $\kappa_{s,f}$, leading to progressively dissimilar profiles at a given timestep, until they asymptotically decay toward zero. The degree of dissimilarity among the solutions is reflected in the “thickness” of the profiles, which is directly determined by the range of $\kappa_{s,f}$ present in the problem.

We initialize an isotropic field $I_f(t = 0, x, \nu, \theta, \phi) = J_f(t = 0, x; t_0 = t_{0,f})$ and allow it to diffuse. We set $t_{0,f} \propto 1/D_f$ to ensure identical initial conditions for every group. We set constants ρ , A , and c to 1 each and use 128 spatial cells distributed in $[-5, 5]$, 100 frequency bins, and 1024×2048 angles to simulate the problem at a rounding tolerance of 10^{-14} (i.e., \sim round-off). Since this problem is positioned well into the diffusive regime, we evolve the transport operator via the Rusanov flux with a wavespeed $S^+ = 0$ (i.e., a pure finite difference). For the test, the scattering opacities $\kappa_{s,f}$ are sampled uniformly from $[1000, \kappa_s^{\max}]$. We study the impact of expanding the range of the uniform distribution on the TT ranks by varying κ_s^{\max} . Increasing this range leads to greater spatial variability in the solution across different frequency groups.

The multigroup Gaussian diffusion problem serves not only as a validation test for the correct implementation of the scattering term in the solver, but also as an important benchmark for assessing the applicability of the multigroup formulation. In the previous tests, the radiation energy density could be written as a simple product of a frequency-

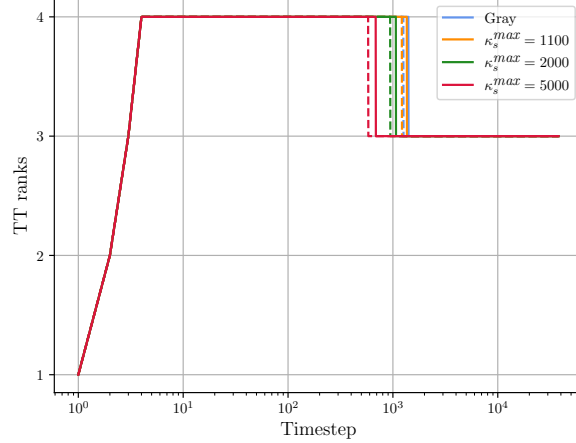


Figure 7. Evolution of TT-ranks for $\kappa_s^{max} = [1000, 1100, 2000, 5000]$. The rank $r_{z\theta}$ is shown with solid lines and $r_{\theta\phi}$ with dashed lines. The ranks initially increase and then decrease as the solution approaches isotropy. Both the rank evolution and compression behavior remain similar across all cases. The minimum compression occurs when the TT ranks are largest and is $\sim 3.5 \times 10^5$.

dependent factor and a spatially dependent factor. In contrast, in Equation (13) the spatial and frequency dimensions are more strongly coupled, suggesting an internal rank of Z greater than one. This coupling makes the problem interesting both in terms of the internal structure of Z and its implications for the resulting TT ranks.

We find that the TT ranks are largely insensitive to changes in spatio-spectral complexity. This behavior is illustrated in Figure 7, which shows the evolution of the TT ranks for $\kappa_s^{max} = 1000, 1100, 2000$, and 5000 .⁸ For each value of κ_s^{max} , TT ranks $r_{z\theta}$ and $r_{\theta\phi}$ are plotted using the same color, with $r_{\theta\phi}$ decreasing first. Although the TT ranks drop at different times, their overall behavior remains similar. We note that this behavior is expected provided that spatio-spectral complexity does not strongly influence the angular dynamics (i.e., the scattering source term maintains \sim isotropy throughout each group’s evolution). Since our TT representation does not exploit separability between the frequency and spatial dimensions, it does not invite rank growth due to the strong space-frequency coupling in this problem—that is, we observe low rank structure as the solution is \sim isotropic over the full spatio-spectral space. The minimum compression observed for this problem is $(\mathcal{C})^{min} \approx 3.5 \times 10^5$ and the speedup achieved is $\mathcal{S} \approx 5865$.

4.4. Multigroup Graziani prompt spectrum (slab version)

The multigroup Graziani problem serves as an excellent benchmark for multigroup implementations and is typically run in 1D spherical geometry (see, e.g., [F. Graziani 2008](#); [Y.-F. Jiang 2022](#)). In this work, we opt for its planar counterpart (i.e., the “slab” version) which equally has analytic solutions ([F. Graziani 2008](#)). This subsection is divided into two main parts. We initially gauge the solver for accuracy and performance on the prompt spectrum problem as described in [F. Graziani \(2008\)](#). In the second part, we test the limits of the solver by adding more complexity to the original problem.

4.4.1. Original formulation

Graziani’s prompt spectrum problem considers an opaque slab with a predefined opacity structure (that of brominated plastic). A boundary condition set to a radiation temperature of $T_s = 0.3$ keV acts on a background with an initial material and radiation temperature of $T_c = 0.03$ keV. 50 frequency groups are used to divide the frequency domain with $\nu_1 = 0.003$ keV and $\nu_{51} = 30$ keV. The medium density is prescribed as 0.0916 g cm^{-3} and the specific heat capacity is set to a exceedingly large value to effectively maintain a constant medium temperature throughout the course of the simulation. We monitor the distribution of radiation energy density among all the different frequency groups at a specific point in space which we call the “fiducial point.” In the examples simulated, we use $N_X = 120$ cells and $N_\theta \times N_\phi = 64 \times 128$ angles and consider a point located at a distance of 2.115×10^{-5} cm from the left boundary

⁸ Note that $\kappa_s^{max} = 1000$ reduces the multigroup problem to a gray problem with uniform scattering opacity.

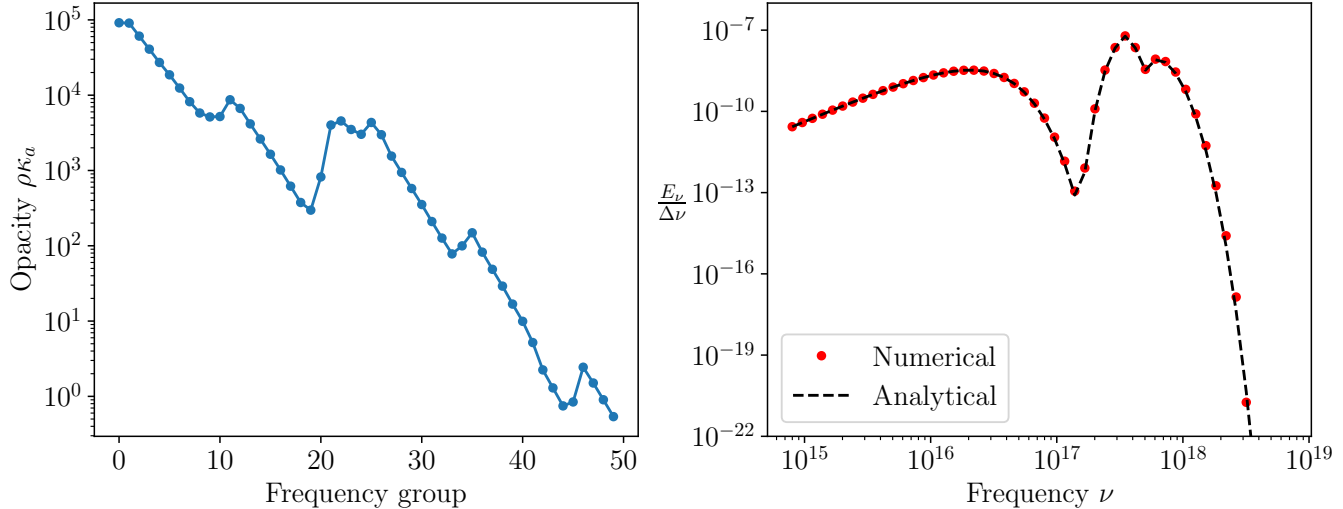


Figure 8. Brominated plastic opacity profile used in the F. Graziani (2008) prompt spectrum problem (left) and comparison between the analytical and TTTT solutions (right). The two peaks observed in the solutions correspond to the maxima of the Planckian emissions from the medium and the boundary. The TTTT solver accurately reproduces the analytic result while achieving compression gains of approximately 296 \times .

to be our fiducial point. All tests in this subsection invoke the HLL flux with $\beta = 20$ (see A. A. Gorodetsky et al. 2025).

The initial energy distribution at the fiducial point is isotropic and takes the shape of a Planckian evaluated at temperature T_c . Since the medium is in thermal equilibrium with the radiation field, the energy distribution remains unchanged until the information from the intensity source at the left boundary reaches it. The energy distribution will eventually converge to the profile as displayed in Figure 8. The first peak arises from the Planckian distribution at the medium temperature T_c , representing thermal emission from the medium itself. The second peak corresponds to the Planckian peak of the source at temperature T_s . Energy at the frequency associated with the source's peak is able to reach the fiducial point more effectively due to the lower opacities at frequencies higher than that peak.

The numerical TT solution was obtained using a rounding tolerance of 10^{-6} and we observe that it captures the analytics accurately while giving compressions and speedups of $\mathcal{C} \approx 296$ and $\mathcal{S} \approx 1.5$.

4.4.2. Spatially varying opacities

Mediums in practical problems might have a mixture of materials scattered throughout space adding more complexities for our solver to resolve. In this test, we set up the Graziani problem with different artificial materials distributed in space. Each material is characterized by a unique opacity structure and as a result, the opacity field varies not only with frequency but also spatially. The frequency dependence follows a power-law trend common to all materials, with random oscillatory components introduced to distinguish individual materials—that is, we logarithmically decrease $\rho\kappa_{a,f}$ from $[10^8, 0.5]$ over frequencies $[\nu_1, \nu_{N_\nu}-1]$ and then add group-wise oscillations with an amplitude sampled from a Gaussian distribution with zero mean and variance $(m \cdot \rho\kappa_{a,f})^2/N_\nu$ where $m = 5$. We vary the number of materials in the medium to consider different levels of complexity in the corresponding opacity fields. The test is conducted with 1, 10, 20, 40, and 120 materials distributed uniformly in space, and we examine the solver's performance for different rounding tolerances. The discretization for these tests was set as $(N_X, N_\nu, N_\theta, N_\phi) \equiv (120, 102, 64, 128)$.

Figure 9 shows the evolution of the TT ranks for varying numbers of materials ($N_{\text{materials}}$) at a rounding tolerance of 10^{-14} (left), as well as the final TT ranks as a function of rounding tolerance for different material counts (right). Rank $r_{z\theta}$ is plotted with a solid line, while $r_{\theta\phi}$ is shown with a dashed line. The curves for different material counts exhibit similar evolution, again indicating that the TT ranks for our selected tensor decomposition are largely insensitive to the spatio-spectral complexity introduced by spatially varying frequency-dependent opacities. Overall, the solver delivers substantial compression compared to a conventional solver representation, \mathcal{C} —with ratios of roughly 121 at a rounding tolerance of 10^{-14} , and rising to about 1985 at a tolerance of 10^{-3} . We also observe speedups ranging from $\mathcal{S} \approx 2$ for a rounding tolerance of 10^{-3} to $\mathcal{S} \approx 1.4$ for a tolerance of 10^{-14} .

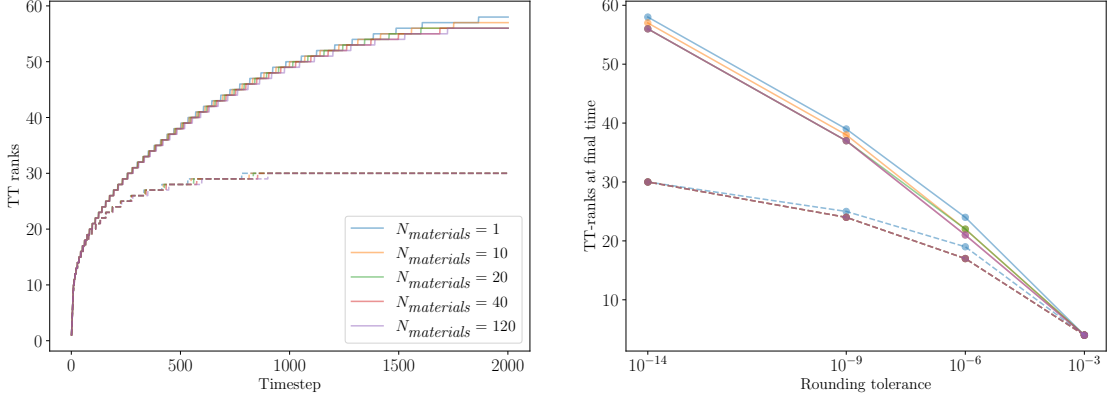


Figure 9. TT-rank evolutions for different $N_{\text{materials}}$ at a rounding tolerance of 10^{-14} (left), and final TT ranks as functions of the rounding tolerance for varying material counts (right). $r_{z\theta}$ is shown with solid lines and $r_{\theta\phi}$ with dashed lines. The near-complete overlap of curves across different material counts indicates that, for the chosen tensor decomposition, the TT ranks are largely insensitive to spatio-spectral complexity arising from spatially varying opacities. The solver achieves significant compression relative to a conventional representation, with compression ratios \mathcal{C} ranging from approximately 121 at a rounding tolerance of 10^{-14} , increasing to about 1985 at a tolerance of 10^{-3} .

4.5. Multigroup stellar irradiation

We extend the gray version of the stellar irradiation problem (M. Klassen et al. 2014; A. A. Gorodetsky et al. 2025) to a multigroup setting. The spatial domain is $[-1000, 1000] \times [-1000, 1000]$ AU. We initialize a circular cold clump with a radius of 267 AU at the origin and 2 radiating stars with radii 8 AU each centered at $[0, -500]$ AU and $[-500, 0]$ AU. The clump and medium temperatures are set to $T = T_r = 1$ K while the stars radiate at $T = T_r = 140$ K. Additionally, the medium, clump, and star densities are assigned values of 10^{-20} , 10^{-16} , and 10^{-12} g cm $^{-3}$ respectively.

The problem is run on a Mac Mini M4 with 310^2 spatial cells, 512×1024 angles, and 20 groups—exceeding a trillion total parameters. We initialize the group opacities so that κ_a increases logarithmically from 10^{-6} at $f = 1$ to 1 at $f = N_\nu/2$, and then decreases logarithmically back to 10^{-6} by $f = N_\nu$. The frequency bounds are set to $(\nu_1, \nu_9) \equiv (10^{12}, 10^{14})$ s $^{-1}$ so that the groups concentrate around the Planckian peak corresponding to the radiation temperature of the stars. Finally, the transport term is computed using the Rusanov flux with a wave speed of $S^+ = c$.

Figure 10 plots $\propto E_f^{1/4}$ for groups 4, 11, 13, and 16 after a \sim steady state is achieved. For $f = 11$, the clump exhibits maximal opacity, leading to the most significant shadowing effect. Radiation penetration increases with distance from the central bins, appearing as partial permeation for $f = 13$ and nearly full permeation for $f = 4$ and $f = 16$. The problem yields \mathcal{C} and \mathcal{S} on the order of $4500\times$ and $232\times$ respectively.

5. DISCUSSION

5.1. Binwise compression

From the above tests, we observe that our solution format requires significantly less storage than the traditional approach. However, an additional question arises: is it more efficient to run a TT-solver and store the solution for each frequency group independently, or to represent the solution across all groups as a single TT object? The first option may seem advantageous when the solutions within certain groups are highly structured and low-rank, thereby reducing the total number of parameters. The second option, on the other hand, enables us to capture and exploit structure along the frequency domain. If the TT solution for bin i has ranks $r_{x\theta}^i$ and $r_{\theta\phi}^i$, we define the number of bin-wise parameters as

$$N_{\text{bin}}^i := N_X r_{x\theta}^i + r_{x\theta}^i N_\theta r_{\theta\phi}^i + r_{\theta\phi}^i N_\phi$$

and the bin-wise compression ratio

$$\mathcal{C}_{\text{bin}}^i := \frac{N_X N_\theta N_\phi}{N_{\text{bin}}^i}.$$

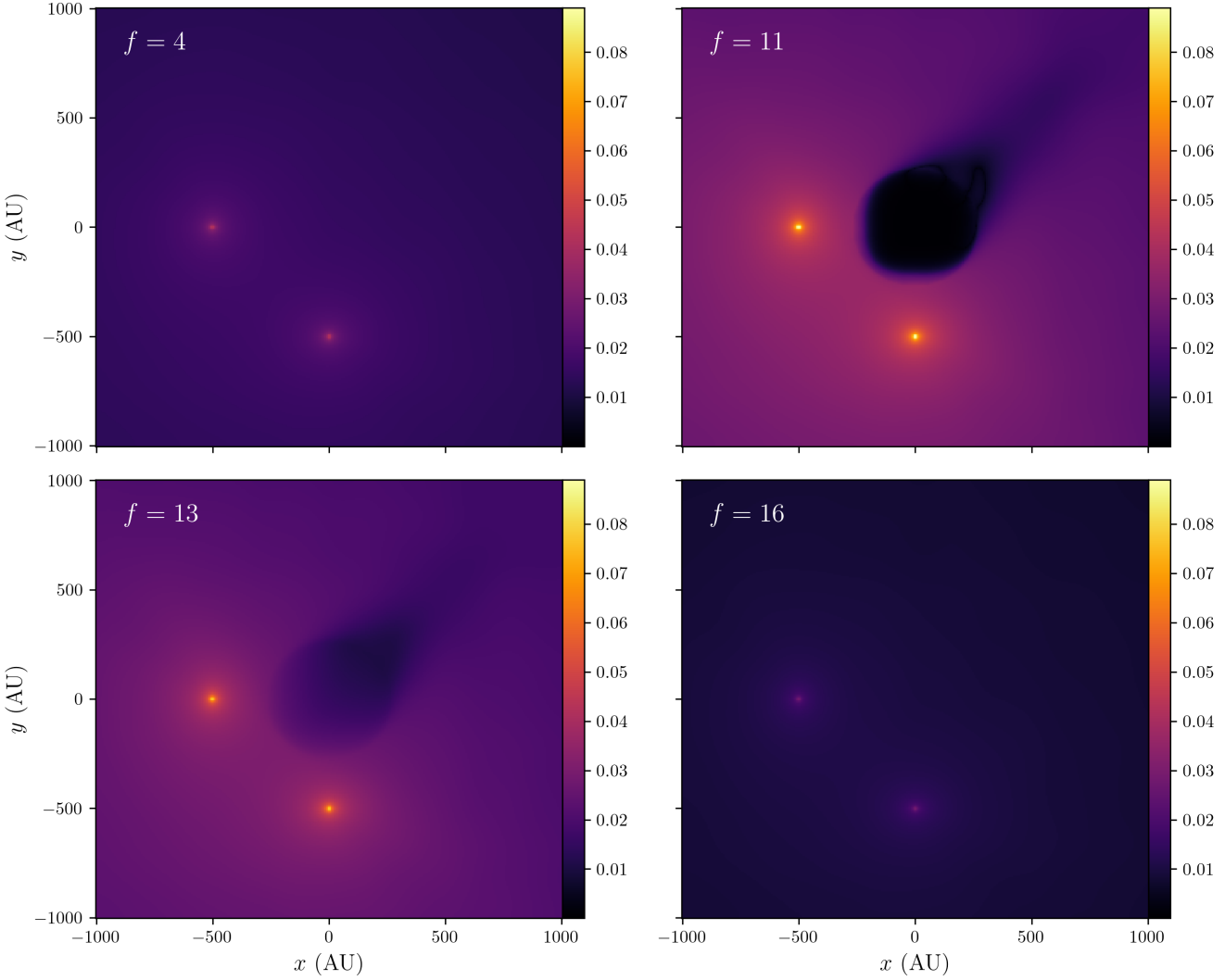


Figure 10. (From top-left in clockwise direction) $\propto E_f^{1/4}$ fields for frequency groups $f = 4, 11, 16$, and 13 . The clump opacity is the greatest for $f = 11$ resulting in a more prominent shadow. Radiation is allowed to permeate as one moves further from the central bins. This can be observed in the form of partial permeation in case of $f = 13$ and almost complete permeation for $f = 4, 15$. We observe compressions and speedups of $\sim 4500\times$ and $280\times$ respectively in this problem.

We present the results for bin-wise compressions in Figure 11 and Table 1. Figure 11 presents a bar plot of \mathcal{C}_{bin}^i for each frequency bin i . These values are obtained by truncating a low-tolerance TT solution in each bin independently at the final time step, using a tolerance of 10^{-9} . For comparison, the multigroup TT solution—evaluated after truncating the same low-tolerance solution at the same final tolerance of 10^{-9} —achieves a compression ratio of $\mathcal{C} = 144$. It is observed that \mathcal{C}_{bin}^i exceeds the multigroup compression ratios in certain bins. However, the aggregate number of parameters required to represent all bin-wise solutions ($= \sum_{i=1}^{N_f} N_{bin}^i$) remains substantially larger than that of the multigroup solution. We also compare the compression behavior with the opacity structure of the problem by plotting scaled opacities in each bin. We comment that the binwise compression pattern follows the opacity distribution. This due to the fact that in bins with larger optical depth, the radiation field becomes more isotropic and yields higher compression by exploiting low-rank structure with respect to the angular domain.

Table 1 summarizes the compression achieved by the multigroup solutions relative to the bin-wise case across three different rounding tolerances— 10^{-6} , 10^{-9} , and 10^{-12} . The results indicate that representing the full multigroup solution as a TT consistently yields superior compression performance compared to running a TT-solver in each bin independently for the one-spatial dimensional Graziani problem considered here. For multi-spatial dimensional

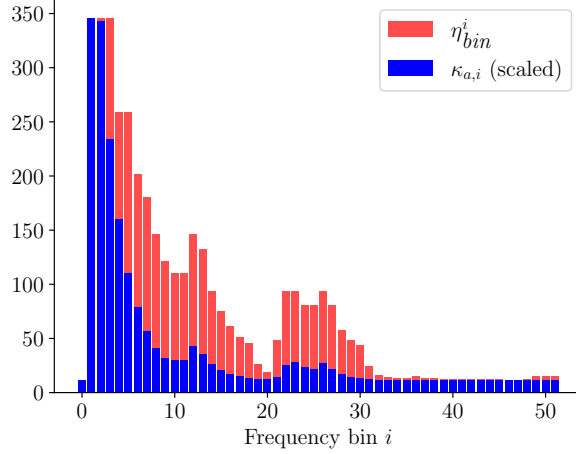


Figure 11. Bar plot of the compression ratio (C_{bin}^i) evaluated for a tolerance of 10^{-9} and the scaled opacity $\kappa_{a,i}$ in each bin i . In some bins, the compression ratio exceeds the multigroup compression $\mathcal{C} = 144$. Nevertheless, the overall compression ratio across all bins is only about 58, which is lower than \mathcal{C} by a factor of 2.5. Another noteworthy observation is that the binwise compression behavior reflects the underlying opacity structure: radiation tends to be more isotropic in optically thicker bins, leading to improved compressibility.

Table 1. Compressions obtained in the multigroup TT representation relative to the bin-wise case across various tolerances.

Tolerance	$\left[\sum_{i=1}^{N_f} N_{bin}^i \right] / N_{TT}$
10^{-3}	1.7
10^{-6}	2
10^{-9}	2.5

problems where $N_X \gg N_\nu, N_\theta$, and N_ϕ , the storage for the extra angular cores required in the binwise approach will be relatively small compared to the storage required for the spatial cores. As a result, the storage requirements for the two approaches may be closer, with the binwise approach possibly winning in some cases where the average $r_{x\theta}^i$ is less than $r_{z\theta}$.

5.2. Internal structure of the combined core

We now examine results concerning the internal structure of the combined core Z and discuss how a low internal rank may be exploited in theory to achieve further compression. We first introduce the notation and definitions used throughout this section. The internal δ -rank of Z is denoted by either $r_{\nu x}$ or $r_{x\nu}$. Figure 12 illustrates these internal ranks, which correspond to the TT ranks that would arise in two different hypothetical formulations with separate TT cores for the space and frequency dimensions (where $r_{\nu x}$ denotes the rank of a hypothetical TT decomposition that leads with the frequency core, and $r_{x\nu}$ denotes the rank of a decomposition that begins with the spatial core). Throughout the remainder of this work, we explicitly distinguish between the TT ranks $r_{z\theta}, r_{\theta\phi}$ and the internal ranks $r_{\nu x}$ and $r_{x\nu}$. One can obtain $r_{\nu x}$ and $r_{x\nu}$ corresponding to a local error tolerance δ by performing a δ -SVD on `reshape`($Z^m, [N_\nu, N_X r_{z\theta}]$) and `reshape`($Z^m, [N_X, N_\nu r_{z\theta}]$) respectively. In both cases, Θ and Φ must be orthogonalized to ensure that the global error is equal to the local one.

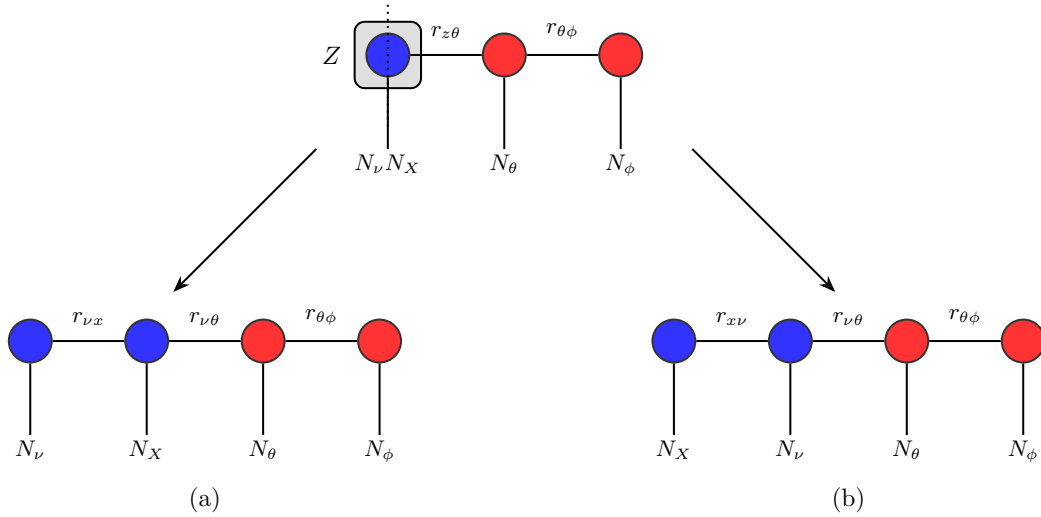


Figure 12. The figure illustrates two possible ways to split the spatio-spectral core Z into separate TT cores for space and frequency. These choices lead to distinct TT topologies with different core orderings and corresponding definitions of the internal ranks. The preference for exploiting $r_{\nu x}$ or $r_{x\nu}$ depends on both the discretization and the problem characteristics. For example, the multigroup hohlraum problem naturally favors topology (a), whereas problems such as stellar irradiation more effectively exploit low-rank structure under topology (b).

Building on the preceding discussion, we introduce additional compression metrics, namely the relative compression ratios

$$\mathcal{C}_{rel}^{\nu} := \frac{N_{TT}}{N_{\nu}r_{\nu x} + N_Xr_{\nu x}r_{z\theta} + N_{\theta}r_{z\theta}r_{\theta\phi} + N_{\phi}r_{\theta\phi}} \quad (14)$$

and

$$\mathcal{C}_{rel}^x := \frac{N_{TT}}{N_Xr_{x\nu} + N_{\nu}r_{x\nu}r_{z\theta} + N_{\theta}r_{z\theta}r_{\theta\phi} + N_{\phi}r_{\theta\phi}}, \quad (15)$$

that quantify the *additional* compression benefits that can be obtained by having separate cores for space and frequency.⁹ \mathcal{C}_{rel}^{ν} is the additional compression obtained by exploiting $r_{\nu x}$ whereas \mathcal{C}_{rel}^x is the additional compression obtained by exploiting $r_{x\nu}$. Comparing \mathcal{C}_{rel}^{ν} and \mathcal{C}_{rel}^x allows us to determine the better TT representation between (a) and (b) in Figure 12 from a compression point of view.

Knowing a priori which TT topology offers superior compressions is often nontrivial. L. Einkemmer et al. (2024) argues that placing “less separable” dimensions (i.e., modes connected by a higher rank) closer together in the TT representation (see Figure 12) tends to improve compression performance. For example, in the optically thin regime (i.e., in the \sim free-streaming limit), the transport operator promotes strong coupling between space and angle potentially leading to limited separability between those dimensions. Problems in this regime, therefore, may benefit from a TT topology that positions the spatial and angular cores “closer” to one another (i.e., adopting internal rank $r_{\nu x}$). Competing, however, is separability between frequency and angle—but in this work, we adopt opacities κ_a and κ_s that are *not* a function of angle, likely promoting high separability between these dimensions. Even under these considerations, the optimal topology is still nuanced as the TT solution size is dependent on problem discretization. For problems where $N_x \gg N_{\nu}, N_{\theta}, N_{\phi}$, topology 12b might be advantageous over 12a as the (likely) dominant $N_Xr_{x\nu}$ term in the denominator of Equation (15) might be significantly smaller than the dominant $N_Xr_{\nu x}r_{z\theta}$ term in the denominator of Equation (14).

⁹ We emphasize again that the extra compression is practically attainable only when the transport and source operators can be applied independently to the space and frequency cores.

We take the opportunity to summarize the solver performance for all test problems by reporting \mathcal{C} and \mathcal{S} , and quantify the compression gains arising from the internal structure of Z through \mathcal{C}_{rel} in Table 2. Below, we discuss some results on the internal ranks $r_{\nu x}$ and $r_{x\nu}$ across all test cases.

Hohlraum and Thermal Relaxation—Irrespective of the boundary condition in the multigroup hohlraum problem or the opacity structure in the thermal relaxation test, the transport physics for each frequency group is independent and results in a solution that is perfectly compressible in frequency. Put differently, for all times one can represent the solution as $k_f \cdot g(x, \theta, \phi)$ where k_f is a frequency-dependent scalar. This implies that $r_{\nu x} = 1$ and Z has high internal structure hence promoting high \mathcal{C}_{rel}^{ν} . The multigroup hohlraum test exhibits $\mathcal{C}_{rel}^{\nu} = 4.9$, meaning that a specialized solver that adopts topology in Figure 12a would permit $4.9 \times$ additional compression. Albeit we see $\mathcal{C}_{rel}^{\nu} = \mathcal{C}_{rel}^x \approx 1$ in the thermal relaxation problem, we note that this problem is effectively purely local and does not require spatial discretization. It is instructive to compare the increase in storage cost for conventional and TT representations when transitioning from a gray to a multigroup formulation in problems that are rank-1 in frequency. In such cases, the storage required by a traditional representation grows linearly with the number of frequency groups N_{ν} , whereas the TT representation in Figure 12a requires only N_{ν} additional parameters beyond those needed for the gray solution. This behavior is intuitive for the hohlraum problem, where each frequency group mirrors the gray dynamics and differs only by a group-dependent scaling factor, which is efficiently captured by the additional N_{ν} parameters in the multigroup TT solution. Finally, we note that although the Hohlraum solution does not admit $r_{x\nu} = 1$, having $r_{\nu x} = 1$ substantially constrains the maximum attainable $r_{x\nu}$. As a result, topology 12b yields compressions that are comparable but smaller ($\mathcal{C}_{rel}^x = 4.8$) than those achieved with topology 12a.

Gaussian Diffusion—We next investigate the evolution of $r_{\nu x}$ and $r_{x\nu}$ for the Gaussian diffusion problem and examine its dependence on the range of scattering opacities employed in the problem. In this problem, the radiation field approaches isotropy, and variations in the internal ranks can therefore be attributed to the spatio-spectral complexity arising from frequency-dependent scattering opacities. The effects of scattering opacity range are observed in Figure 13 where we plot the evolution of the internal ranks for different values of κ_s^{max} . The initial solution is identical for each group and is therefore a rank-1 TT. The ranks increase as the solutions begin to diverge inside different groups at varying rates due to different values of $\kappa_{s,f}$. The radiation energy asymptotically approaches zero across all frequency groups, leading to a decrease in $r_{\nu x}$ and $r_{x\nu}$. We also remark that the internal ranks attain a greater maximum value when the span of opacities present in the problem is large. A wider range yields less similar solution profiles across different groups and therefore leads lower internal structure within Z . The observed values of $r_{\nu x}$ and $r_{x\nu}$ remain low despite the use of randomly sampled opacities, indicating structure within Z . In general, we find that \mathcal{C}_{rel}^{ν} is greater than \mathcal{C}_{rel}^x . The difference, however, is small (i.e., both lie in the range of 2 to 3). Due to global \sim isotropy in this problem, separability in space-angle and frequency-angle is unlikely to provide an advantage for a TT topology with internal rank $r_{\nu x}$. Alongside the above considerations, a discretization with $N_X \simeq N_{\nu}$ suggests little difference in compression performance between the two topologies, consistent with our observations.

Graziani Prompt Spectrum—We assess the internal rank behavior for Graziani’s prompt spectrum problem with spatially varying opacities where the number of materials in the problem is equal to the matrix-rank of the absorption opacity field, i.e., $\text{rank}(\rho\kappa_{a,f}) = N_{\text{materials}}$ with $\rho\kappa_{a,f} \in \mathbb{R}^{N_X \times N_{\nu}}$. Since $\text{rank}(\rho\kappa_{a,f})$ directly influences the growth of the internal ranks, we anticipate that $N_{\text{materials}}$ will affect the internal rank behavior. Figure 14 summarizes these results, showing the evolution of the internal ranks in the left plots and their variation with respect to δ on the right, for six test cases with 1, 5, 10, 20, 40, and 100 materials distributed in space. As expected, these ranks increase with larger $N_{\text{materials}}$ and tighter tolerances δ . For high material counts and small δ , $r_{\nu x}$ remains well below its full rank $\min(N_{\nu}, N_X N_{\theta} N_{\phi})$ whereas $r_{x\nu}$ reaches its full rank $\min(N_X, N_{\nu} N_{\theta} N_{\phi})$. The stronger low-rank structure in the former yields larger relative compression ratios, with \mathcal{C}_{rel}^{ν} decreasing from 2.9 at $N_{\text{materials}} = 1$ to 2 at $N_{\text{materials}} = 100$, compared to \mathcal{C}_{rel}^x , which drops from 2.1 to 1 over the same range. In the Graziani prompt spectrum test, more pronounced deviations away from global isotropy disfavor separability in space and angle, thereby encouraging a TT topology with $r_{\nu x}$ (reflected in $\mathcal{C}_{rel}^x < \mathcal{C}_{rel}^{\nu}$). We conclude by noting that, under the current tensor decomposition, the TT ranks remain largely insensitive to opacity-driven complexity, whereas the internal ranks reflect these effects. Furthermore, for problems exhibiting strong coupling between space and frequency, splitting the spatio-spectral core offers little to no additional benefit.

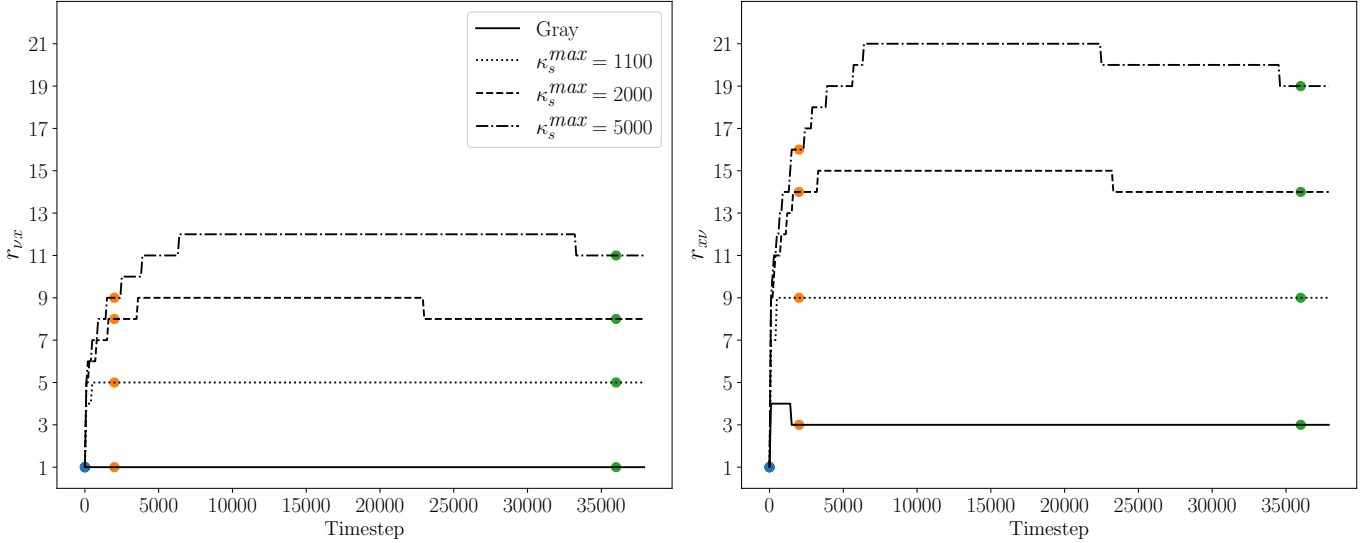


Figure 13. Evolution of the internal rank $r_{\nu x}$ (left) and r_{xv} (right) for progressively larger ranges of $\kappa_{s,f}$. Colored markers indicate the ranks at time steps 1, 2000, and 38000 with the corresponding solutions at these times shown in Figure 6. The internal ranks grows from its initial value of 1 as the groups begin to diffuse at different rates, reaches a peak, and subsequently decreases as the solution decays toward zero. We emphasize that a wider spread in opacities leads to greater dissimilarity among the groupwise solutions, necessitating higher TT ranks for accurate representation. This trend is reflected in the growth of the maximum value achieved by $r_{\nu x}$ and r_{xv} as the opacity range is increased.

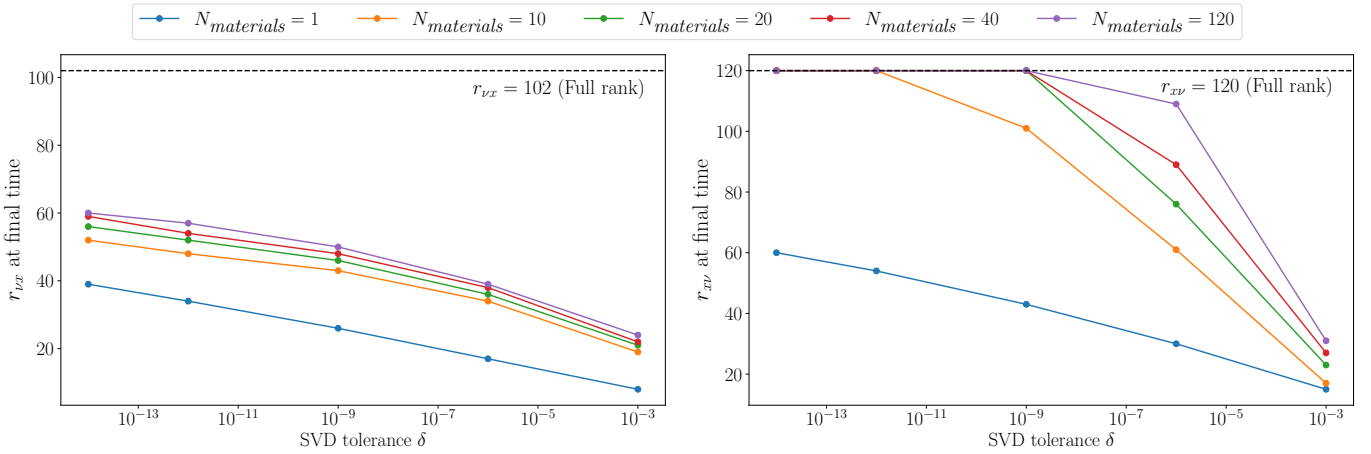


Figure 14. Evolution of the internal ranks (left) and their dependence on the SVD tolerance δ (right) for test cases with 1, 5, 10, 20, 40, and 100 spatially distributed materials and a rounding tolerance of 10^{-14} . The internal ranks grow with increasing $N_{\text{materials}}$ and tighter δ . We observe that $r_{\nu x}$ always remains well below its full rank, demonstrating low-rank internal structure within Z despite the problem’s complexity. On the other hand, r_{xv} approaches its full rank for lower values of δ . This is reflected in the relative compression numbers which tend to be higher for TT-topology in Figure 12a compared to the one in Figure 12b.

Stellar Irradiation—The stellar irradiation problem, which demands fine spatial and angular resolution and would ordinarily incur prohibitive storage costs, benefits substantially from the TT representation, as evidenced by the high \mathcal{C} ($= 4583$). Outside the central clump, the optically thin background promotes strong space-angle coupling (i.e., in the \sim free-streaming limit), thereby favoring a TT topology with $r_{\nu x}$. Nevertheless, we observe $\mathcal{C}_{\text{rel}}^{\nu} = 2$ and $\mathcal{C}_{\text{rel}}^x = 7$. We hypothesize that the higher $\mathcal{C}_{\text{rel}}^x$ is likely due to a combination of spatial symmetry in the solution about the 45° diagonal and the fact that $N_X \gg N_{\nu}$. Consequently, the dominant storage cost in both topologies scales with N_X ; however, in topology 12a this term is weighted by only one rank r_{xv} , yielding superior compression.

Table 2. Summary of results for all test cases presented in Section 4. The table reports solver settings, including the rounding tolerance and SVD tolerance δ , along with performance metrics such as the minimum compression ratios, defined in (12), (14), and (15), over the course of the simulation as well as the achieved speedup \mathcal{S} . The file sizes of the solutions at $(\mathcal{C})^{\min}$ are also reported. The consistently high total and relative compression ratios demonstrate that, in addition to using a TT representation, employing a separate frequency core is advantageous in most cases. The dashes in the Hohraum and thermal relaxation results signify insensitivity to tolerance value.

Test	Case	N_x	N_ν	N_θ	N_ϕ	Rounding tol	SVD tol δ	$(\mathcal{C})^{\min}$	$(\mathcal{C}_{\text{rel}}^{\nu})^{\min}$	$(\mathcal{C}_{\text{rel}}^x)^{\min}$	\mathcal{S}	File size
Hohraum 2d	$I_{f,\text{init}} = \varepsilon_f(T_{\text{init}})$	128 ²	10	512	1024	10^{-4}	—	5150	4.9	4.8	60	134 MB
Hohraum 2d	$I_{f,\text{init}} = 1/N_\nu$	128 ²	10	512	1024	10^{-4}	—	5150	4.9	4.8	60	134 MB
Thermal relaxation	$N_\nu = 3$	4	3	512	1024	—	—	4000	1	1	0.8	14 KB
Thermal relaxation	$N_\nu = 100$	4	100	512	1024	—	—	10^5	1.18	1.18	25	21 KB
Gaussian diffusion	$\kappa_s^{\max} = 1000$	128	100	1024	2048	10^{-8}	10^{-12}	3.5×10^5	3	2.8	5865	916 KB
Gaussian diffusion	$\kappa_s^{\max} = 1100$	128	100	1024	2048	10^{-8}	10^{-12}	3.5×10^5	2.7	2.6	5865	916 KB
Gaussian diffusion	$\kappa_s^{\max} = 2000$	128	100	1024	2048	10^{-8}	10^{-12}	3.5×10^5	2.6	2.5	5865	916 KB
Gaussian diffusion	$\kappa_s^{\max} = 5000$	128	100	1024	2048	10^{-8}	10^{-12}	3.5×10^5	2.5	2.2	5865	916 KB
Graziani	F. Graziani (2008)	120	52	64	128	10^{-6}	10^{-9}	296	2	2.1	1.5	1.5 MB
Graziani	$N_{\text{materials}} = 1$	120	102	64	128	10^{-6}	10^{-9}	308	3	2.3	2	2.8 MB
Graziani	$N_{\text{materials}} = 10$	120	102	64	128	10^{-6}	10^{-9}	308	2	1.1	2	2.6 MB
Graziani	$N_{\text{materials}} = 20$	120	102	64	128	10^{-6}	10^{-9}	308	1.9	1	2	2.6 MB
Graziani	$N_{\text{materials}} = 40$	120	102	64	128	10^{-6}	10^{-9}	308	1.9	1	2	2.5 MB
Graziani	$N_{\text{materials}} = 120$	120	102	64	128	10^{-6}	10^{-9}	308	1.8	1	2	2.5 MB
Stellar irradiation	—	310^2	20	512	1024	10^{-3}	10^{-3}	4583	2	7	232	1.8 GB

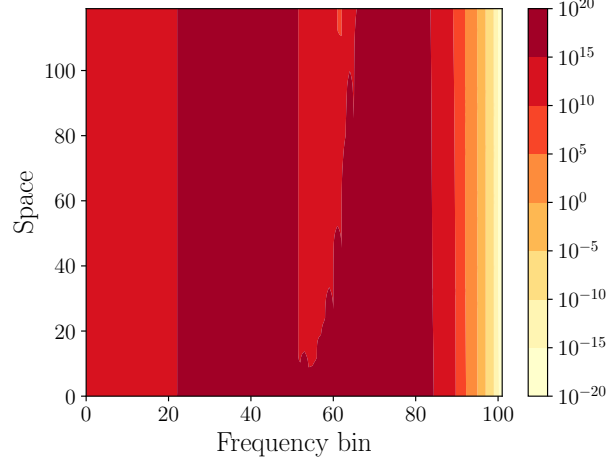


Figure 15. Mean intensity field produced by our solver for the 10-material case. This captures all the spatio-spectral interactions as opposed to the results shown in Figure 16a, where the internal rank of Z is limited to a tolerance δ .

5.3. Pointwise errors

The internal rank of Z is evaluated for some error tolerance δ using an SVD-based procedure that approximates the solution while ensuring that the relative Frobenius norm error is smaller than δ .¹⁰ This approximation is obtained by truncating smaller singular values based on the tolerance and roughly has the effect of limiting the accuracy of the solution to a window extending from the maximum value down to approximately the product of the tolerance and the maximum value. Outside this range, pointwise errors may be incurred up to the relative error. We quantify these pointwise errors by introducing the error field $\gamma(\delta)$ which is the relative error between the mean intensity from the TT solver and the mean intensity when the internal rank of Z is limited by tolerance δ .

The effect of these pointwise errors can be observed in Graziani's problem, where initializing the specific intensity I with a Planck distribution produces a broad range of values in I . Figure 15 shows the mean intensity from our solver and sub-figures 16a, 16b, and 16c display the mean intensity field, error field $\gamma(\delta)$, and mean intensity at a fixed spatial point respectively when the internal rank $r_{\nu x}$ is constrained by δ . The results are obtained for $\delta = 10^{-9}$, 10^{-6} , and 10^{-3} while the TT-rounding tolerance is fixed at 10^{-6} for all cases. These results highlight how the value of δ can constrain the dynamic range of the solution that is accurately captured. For instance, in the $\delta = 10^{-6}$ case (last row), values outside the interval from 10^{18} (the maximum) down to $10^{18-6} = 10^{12}$ show numerical artifacting: white patches in column 1 correspond to negative values, which appear as oscillations in the log-log plot of column 3. Furthermore, the error surpasses 1 outside this range, as seen in column 2. The reduction in observed artifacts as δ decreases indicates that tighter tolerances provide a more accurate solution over a larger dynamic range. While we present results only for $r_{\nu x}$, similar patterns are observed for $r_{x\nu}$.

The pointwise errors in the mean intensity are strongly dependent on δ , highlighting a tradeoff between increased compression and the fidelity of the mean intensity field. Nonetheless, a larger δ may be acceptable if the application does not demand resolving such a wide dynamic range. We end this discussion by reiterating that these artifacts do not occur in our solver and appear only when the internal δ -rank of Z is leveraged by splitting it into separate space and frequency cores.

5.4. Trade-offs and Implications

Despite the attractive potential for additional compression afforded by splitting Z , we choose to not pursue this approach in the present work due to practical feasibility considerations discussed earlier—that is, several key quantities, such as opacities and emissivities, depend simultaneously on space and frequency, and these quantities must have the same format as the TT solution in order to interact through standard TT operations. If the TT solution were to employ separate spatial and frequency cores, the spatio-spectral quantities would first need to be split accordingly before being added to or multiplied with the solution. This process introduces additional singular value decompositions, along with

¹⁰ In a hypothetical implementation that splits the combined core Z , the SVD tolerance δ would be equivalent to the rounding tolerance used to truncate $r_{\nu x}/r_{x\nu}$.

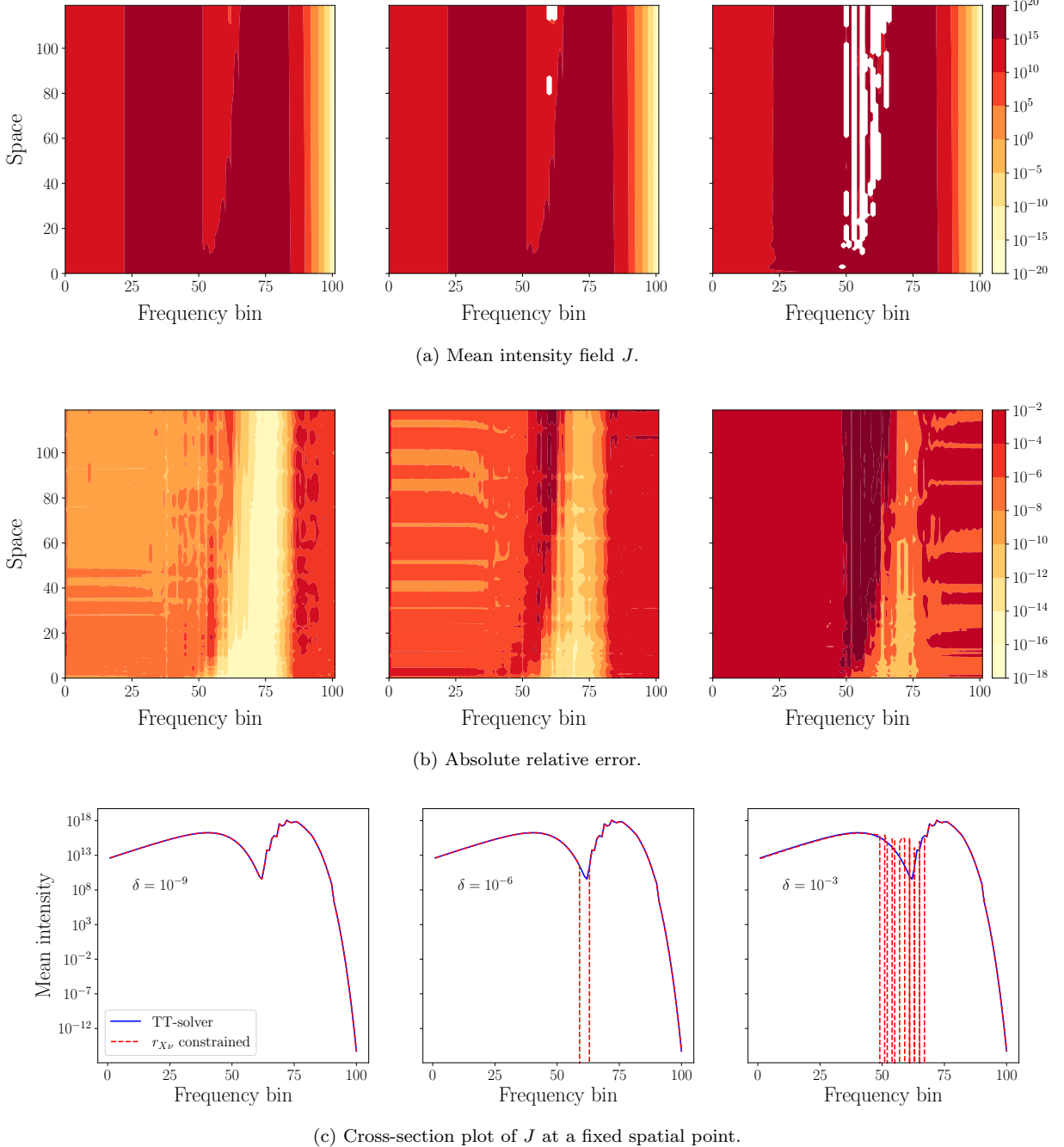


Figure 16. Mean intensity and error plots for the 10-material case when the internal rank $r_{\nu x}$ is constrained using δ . The left, center, and right plots correspond to $\delta = 10^{-9}$, 10^{-6} , and 10^{-3} , respectively. White regions in the contour plots indicate negative values, which appear as small oscillations in the cross-section plots. These errors diminish as δ decreases.

the associated truncation errors and computational overhead. Such costs can become prohibitive, particularly if SVDs must be performed at every time step.

Besides implementation concerns, there are other potential issues which preclude us from splitting Z . For scenarios exhibiting significant spatio-spectral complexity, such as those arising from intricate opacity structures, the additional compression advantage diminishes. Furthermore, pointwise errors are observed in the radiation energy profiles for the fully low-rank case. This behavior arises because Planckian distributions can introduce large variations in magnitude depending on the discretization of the frequency domain—specifically, the integrated Planckian values within bins can

vary substantially based on their proximity to the spectral peak. Although this effect is generally negligible, in highly complex setups (e.g., Graziani’s problem with spatially varying opacities), the finite precision of singular values in SVD-based operations such as rounding can lead to localized discrepancies. Nonetheless, the relative Frobenius norm of such errors remains bounded below a user-defined tolerance, ensuring controlled numerical accuracy.

6. CONCLUSION

In this work, we have presented an algorithm to solve the multigroup radiation transport equation using a TT-solver. Our solver employed a TT decomposition that contained a single “merged” TT core for the spatial and frequency dimension. We tested our solver on a variety of test problems and analyzed its performance.

High compression ratios were consistently achieved with the TT solver across all test cases. The gray versions of the hohlraum, thermal relaxation ($N_\nu = 100$), and Gaussian diffusion problems covered in [A. A. Gorodetsky et al. \(2025\)](#) achieve compressions of approximately 3×10^3 , 1300, and 1.7×10^4 , respectively, relative to their traditional gray representations. In this work, we observe even larger compressions when applying the multigroup TT solver to these problems’ frequency-dependent counterparts at the same discretization and rounding tolerance. The reason is that the multigroup TT solution exploits correlations not only between spatial and angular dimensions, as in the gray case, but also between frequency and angular dimensions, thereby maintaining relatively low TT ranks. While the multigroup TT representation does require more parameters than its gray counterpart, this increase is lower compared to the traditional storage cost, which scales linearly with N_ν .

In addition, we also examined the low-rank structure within the combined space–frequency core Z as a potential source of further compression. We introduced two different definitions of the internal rank ($r_{\nu x}$ and $r_{x\nu}$) and linked them to alternative TT core orderings in which space and frequency are represented by separate cores (Figure 12). We studied their behavior in all test problems and compared the additional compression obtained by exploiting either of these internal ranks. For the hohlraum, Gaussian diffusion, and Graziani problems, topology 12a proved more efficient, whereas the stellar irradiation problem was better represented by topology 12b. We note that while additional compression is possible, its effectiveness depends on both the feasibility of applying transport and source operators in low-rank form and the underlying problem complexity. In cases with strong spatio-spectral coupling, such as complex opacity fields, the gains diminish, and small pointwise errors may appear due to SVD truncation effects.

Several aspects of the problem remain unexplored in this study. We briefly outline some of these limitations and potential directions for future work. First, no systematic strategy was used to partition the frequency domain into groups. The specific choice of bins, together with the associated radiation dynamics, directly influences the TT ranks, but the impact of this choice has not been examined here.

Second, we have only partially explored the topic of alternate TT-core orderings in our internal rank study. We concede that there are many possibilities that have not been investigated in this work. For example, a TT solution that adopts a $Z\Phi\Theta$ ordering as opposed to our $Z\Theta\Phi$ ordering might offer improved compression. We remark that identifying the optimal core ordering, or more broadly, the optimal tensor-network topology for high-dimensional data remains a challenging and open problem in the tensor-network literature.

Finally, we acknowledge that our solver does not take advantage of the low-rank structure of Z , owing to the absence of a feasible approach for applying the HLL transport and source operators to a TT solution with separated space and frequency dimensions. Potential remedies include randomized SVD techniques or cross-approximation–based methods, which we leave for future investigation.

ACKNOWLEDGMENTS

A.D and A.A.G were supported by the Los Alamos National Laboratory (LANL) under the project “Algorithm/Software/Hardware Co-design for High Energy Density applications” at the University of Michigan. A.D. was also supported, in part, by AFOSR Computational Mathematics Program under the Award #FA9550-24-1-0246 to study the performance of randomized rounding in the MRT context. P.D.M, J.C.D, C.D.M., J.M.M., and L.F.R. were supported by LANL under the M³AP project. LANL is operated by Triad National Security, LLC, for the National Nuclear Security Administration of U.S. Department of Energy (Contract No. 89233218CNA000001). This document is approved for unlimited release under LA-UR-26-20665.

REFERENCES

Biamonte, J., & Bergholm, V. 2017, arXiv preprint arXiv:1708.00006

Caballero, I., & Wilms, J. 2012, X-ray pulsars: a review, <https://arxiv.org/abs/1206.3124>

Chevalier, R. A., & Fransson, C. 2008, ApJL, 683, L135, doi: 10.1086/591522

Einkemmer, L., Kormann, K., Kusch, J., McClaren, R. G., & Qiu, J.-M. 2024, arXiv e-prints, arXiv:2412.05912, doi: 10.48550/arXiv.2412.05912

Giron, I., Krief, M., Stone, N. C., & Steinberg, E. 2026, arXiv e-prints, arXiv:2601.05120, doi: 10.48550/arXiv.2601.05120

Goldberg, J. A., Jiang, Y.-F., & Bildsten, L. 2022, ApJ, 933, 164, doi: 10.3847/1538-4357/ac75e3

González, M., Vaytet, N., Commerçon, B., & Masson, J. 2015, A&A, 578, A12, doi: 10.1051/0004-6361/201525971

Gorodetsky, A. A., Mullen, P. D., Deshpande, A., et al. 2025, arXiv e-prints, arXiv:2503.18056, doi: 10.48550/arXiv.2503.18056

Graziani, F., ed. 2008, Lecture Notes in Computational Science and Engineering, Vol. 62, Computational Methods in Transport: Verification and Validation (Springer), doi: 10.1007/978-3-540-77362-7

Haines, B. M., Keller, D. E., Long, K. P., et al. 2022, Physics of Plasmas, 29, 083901, doi: 10.1063/5.0100985

Huang, X., Meza, M. R., Yun, S. B., et al. 2025, arXiv e-prints, arXiv:2512.12985, doi: 10.48550/arXiv.2512.12985

Jiang, Y.-F. 2021, ApJS, 253, 49, doi: 10.3847/1538-4365/abe303

Jiang, Y.-F. 2022, Multi-group Radiation Magneto-hydrodynamics based on Discrete Ordinates including Compton Scattering, <https://arxiv.org/abs/2209.06240>

Jiang, Y.-F., Blaes, O., Kaul, I., & Zhang, L. 2025, ApJ, 988, 43, doi: 10.3847/1538-4357/addecb

Jiang, Y.-F., Stone, J. M., & Davis, S. W. 2014, ApJS, 213, 7, doi: 10.1088/0067-0049/213/1/7

Kim, Y., Di Stefano, C., Kozlowski, P. M., et al. 2023, Physics of Plasmas, 30, 112701, doi: 10.1063/5.0156374

Klassen, M., Kuiper, R., Pudritz, R. E., et al. 2014, ApJ, 797, 4, doi: 10.1088/0004-637X/797/1/4

Liu, H., Jiang, Y.-F., Quataert, E., Greene, J. E., & Ma, Y. 2025, ApJ, 994, 113, doi: 10.3847/1538-4357/ae0c19

Menon, S. H., Federrath, C., & Krumholz, M. R. 2023, Monthly Notices of the Royal Astronomical Society, 521, 5160

Mills, B. S., Davis, S. W., Jiang, Y.-F., & Middleton, M. J. 2024, ApJ, 974, 166, doi: 10.3847/1538-4357/ad6b21

Nedora, V., Crosato Menegazzi, L., Peretti, E., Dietrich, T., & Shibata, M. 2025, Monthly Notices of the Royal Astronomical Society, 538, 2089

Oseledets, I. V. 2011, SIAM Journal on Scientific Computing, 33, 2295

Proga, D. 2007, arXiv preprint astro-ph/0701100

Proga, D., Stone, J. M., & Drew, J. E. 1999, MNRAS, 310, 476, doi: 10.1046/j.1365-8711.1999.02935.x

Proga, D., Stone, J. M., & Kallman, T. R. 2000, ApJ, 543, 686, doi: 10.1086/317154

Rosen, A. L., & Krumholz, M. R. 2020, AJ, 160, 78, doi: 10.3847/1538-3881/ab9abf

Rosen, A. L., Krumholz, M. R., McKee, C. F., & Klein, R. I. 2016, Monthly Notices of the Royal Astronomical Society, 463, 2553

Roughan, M. 2020, The Polylogarithm Function in Julia, <https://arxiv.org/abs/2010.09860>

Ryan, B. R., & Dolence, J. C. 2020, ApJ, 891, 118, doi: 10.3847/1538-4357/ab75e1

Secunda, A., Jiang, Y.-F., & Greene, J. E. 2024, ApJL, 965, L29, doi: 10.3847/2041-8213/ad34b0

Secunda, A., Jiang, Y.-F., & Greene, J. E. 2025, ApJ, 984, 19, doi: 10.3847/1538-4357/adc25b

Sekora, M. D., & Stone, J. M. 2010, J. Comput. Phys., 229, 6819, <https://api.semanticscholar.org/CorpusID:33501797>

Shlosman, I., Vitello, P. A., & Shaviv, G. 1985, ApJ, 294, 96, doi: 10.1086/163278

Thompson, C. 1994, Monthly Notices of the Royal Astronomical Society, 270, 480

Tolkach, V., Morozov, V., & Hassanein, A. 2003, Development of comprehensive models for opacities and radiation transport for IFE systems., Tech. rep., Argonne National Lab., Argonne, IL (US)

Toro, E. F. 2009, Riemann Solvers and Numerical Methods for Fluid Dynamics (Springer Berlin Heidelberg), doi: 10.1007/b79761

Voigt, A. 2022, Comparison of methods for the calculation of the real dilogarithm regarding instruction-level parallelism, <https://arxiv.org/abs/2201.01678>

Voigt, A. 2023, An algorithm to approximate the real trilogarithm for a real argument, <https://arxiv.org/abs/2308.11619>

White, C. J., Mullen, P. D., Jiang, Y.-F., et al. 2023, ApJ, 949, 103, doi: 10.3847/1538-4357/acc8cf

Wollaeger, R. T., van Rossum, D. R., Graziani, C., et al. 2013, The Astrophysical Journal Supplement Series, 209, 36

Wünsch, R. 2024, *Frontiers in Astronomy and Space Sciences*, 11, 1346812, doi: [10.3389/fspas.2024.1346812](https://doi.org/10.3389/fspas.2024.1346812)

Zhang, L., Stone, J. M., Mullen, P. D., et al. 2025, *ApJ*, 995, 26, doi: [10.3847/1538-4357/ae0f91](https://doi.org/10.3847/1538-4357/ae0f91)
Zrake, J., Beloborodov, A. M., & Lundman, C. 2019, *The Astrophysical Journal*, 885, 30